

First- and second-order Raman spectroscopy of monoclinic β -Ga₂O₃

Benjamin M. Janzen ¹, Roland Gillen ², Zbigniew Galazka ³, Janina Maultzsch,² and Markus R. Wagner ^{1,*}

¹Technische Universität Berlin, Institute of Solid State Physics, Hardenbergstraße 36, 10623 Berlin, Germany

²Friedrich-Alexander Universität Erlangen-Nürnberg, Staudtstraße 7, 91058 Erlangen, Germany

³Leibniz-Institut für Kristallzüchtung, Max-Born-Straße 2, 12489 Berlin, Germany



(Received 21 January 2022; accepted 20 April 2022; published 24 May 2022)

We employ a combined experimental-theoretical study of the first- and second-order Raman modes of monoclinic β -Ga₂O₃. Gallium oxide has attracted considerable interest due to its deep-UV band gap paired with a high critical field strength, offering promising applications in power electronics. A crucial prerequisite for the future development of Ga₂O₃-based devices is a detailed understanding of the lattice vibrations, i.e., phonons, as they govern important material properties such as elasticity, thermal conductivity, temperature-dependence of the band gap, or free-carrier transport. Polarized micro-Raman spectroscopy measurements on the (010) and ($\bar{2}01$) planes of β -Ga₂O₃ single crystals enable the determination of the phonon frequencies of all 15 first-order and more than 40 second-order Raman modes. The experimental results are correlated with calculations of the mode frequencies, the phonon dispersion relation, and the phonon density of states using density functional perturbation theory. By applying a group-theoretical analysis, we are able to distinguish between overtones and combinational modes and identify the high-symmetry points in the Brillouin zone that contribute to the observed second-order modes. Based on this information, we demonstrate the simultaneous determination of Raman, IR, and acoustic phonons in β -Ga₂O₃ by second-order Raman spectroscopy.

DOI: [10.1103/PhysRevMaterials.6.054601](https://doi.org/10.1103/PhysRevMaterials.6.054601)

I. INTRODUCTION

The properties of crystalline materials are strongly affected by their structure and lattice dynamics. The phonons specifically impact the elasticity (acoustic phonons), the thermal conductivity (heat carried by phonons), the free-carrier transport (via phonon scattering) and they are crucial in the temperature dependence of the optical band gap (influenced by electron-phonon coupling). A powerful tool to investigate the vibrational properties of crystalline materials is inelastic light-scattering spectroscopy, in particular Raman scattering for optical phonons and Brillouin light scattering for acoustic phonons. The majority of the Ga₂O₃-related Raman studies have focused on the thermodynamically most stable monoclinic β polymorph [1–9], although a set of polarized Raman spectra of the orthorhombic κ (also referred to as ϵ) [10] phase was recently reported [11]. The first-order Raman spectra of β -Ga₂O₃ single crystals were already demonstrated by Dohy *et al.* [2]. The authors employed temperature-dependent Raman spectroscopy to study the influence of the lattice expansion. In conjunction with valence force-field calculations, they identified three categories of Raman-active phonons with respect to the motions of Ga and O atoms. A following work by Machon *et al.* [3] carried out Raman spectroscopy in diamond anvil cells, revealing a transition from the β - to the α -phase under high pressure. The first set of polarized Raman spectra of β -Ga₂O₃, which was able to distinguish all 15 Raman-active phonon modes of different vibrational symmetries, was reported by Onuma *et al.* [5]. Fiedler *et al.*

[12] investigated the effects of high Si- or Sn-doping concentrations on the first-order Raman spectra of β -Ga₂O₃, and they observed a number of additional Raman peaks, whose excitations were assigned to (i) electronic excitations involving the impurity band formed by effective-mass-like hydrogenic shallow donors, (ii) nonhydrogenic donors, or (iii) the phonon-plasmon coupling associated with infrared-active modes. Yao *et al.* [9] employed Raman spectroscopy and Raman spectral mapping as a nondestructive method to evaluate the crystallinity and uniformity of single-crystal β -Ga₂O₃ grown by the edge-defined film-fed growth (EFG) method. Similarly, in a pair of studies, Zhang *et al.* employed confocal [7] and temperature-dependent [8] Raman spectroscopy to investigate Si-, Mg-, Fe-, and Sn-doped EFG-grown β -Ga₂O₃, proving superior crystallinity and high uniformity of both the undoped and doped Ga₂O₃ substrates. The authors revealed frequency shifts and intensity variations of the intrinsic Raman modes upon doping, which were ascribed to the substitution of dopants on Ga lattice sites [7]. Moreover, they revealed that both the Raman frequencies and the full widths at half-maximum (FWHMs) of the individual Raman modes scaled linearly with temperature in a range between 77 and 297 K for both the doped and undoped samples [8]. In a subsequent study, Seyidov *et al.* [13] applied Raman spectroscopy of Mg- and Si-doped bulk β -Ga₂O₃ crystals grown by the Czochralski method. Exclusively for the Mg-doped sample, the authors observed an additional Raman peak at 5150 cm⁻¹, which was attributed to resonant electronic Raman scattering (ERS) produced by Ir⁴⁺ ions. The impact of the individual lattice sites on the Raman spectra was further investigated by Janzen *et al.* [6], who studied β -Ga₂O₃ in two different oxygen isotope compositions (¹⁶O, ¹⁸O).

*markus.wagner@physik.tu-berlin.de

Quantifying the mode frequency shifts of all Raman modes observed for the ^{18}O with respect to the ^{16}O spectra enabled us to identify (i) the atomistic origin of all modes (Ga-Ga, Ga-O, or O-O), as well as (ii) the Raman modes that were dominated by the different, inequivalent O- or Ga-atoms of the unit cell. Moreover, Kranert *et al.* [1] experimentally determined the Raman tensor elements in the framework of a modified Raman tensor formalism proposed in their preceding study [14]. Aside from the Raman-active phonons, IR-active phonons constitute an important class of lattice vibrations with different symmetries, and they were treated theoretically in a number of publications [2,4,15–18]. Experimental access to infrared-active TO-phonons was first provided by Dohy *et al.* [2] by employing IR transmittance spectroscopy. The results were confirmed and extended by Villora *et al.* [18], who applied IR reflectance spectroscopy. Liu *et al.* [4] provided first principles of IR-active phonons and their assignments to mode symmetries, the results of which were confirmed and refined by Mengle and Kioupakis [17]. The two consecutive works of Onuma *et al.* [15] and Schubert *et al.* [16] added experimental determination of the LO-phonons by using IR ellipsometry.

Nevertheless, the simultaneous detection of IR- and Raman-active phonons is not possible using ellipsometry or first-order Raman spectroscopy. One possibility to overcome this issue is second-order Raman spectroscopy (also referred to as two-phonon Raman scattering), in which two single phonons interact with an incident photon to produce Raman overtones or sum (difference) frequency combinations. While analogously to first-order Raman scattering energy and momentum conservation must apply for this scattering process, the momentum conservation condition permits the participation of phonons with arbitrary wave vectors. Consequently, the restriction to Γ -point phonons, as is the case in first-order Raman experiments, is lifted, allowing not only to probe Raman-active phonons from across the Brillouin zone, but also to study the IR-active phonons previously inaccessible in first-order Raman scattering. Whereas second-order Raman scattering has been thoroughly investigated for cubic [19–24] and hexagonal [25–31] crystals, studies on monoclinic systems are scarce.

Using high-resolution polarized micro-Raman spectroscopy to probe bulk $\beta\text{-Ga}_2\text{O}_3$ single crystals grown by the Czochralski method [32–34], we provide a comprehensive study of first- and second-order Raman spectra. Phonon modes of different vibrational symmetries are separated by selected polarization configurations of incident and scattered light. Aside from determining the symmetry groups of the high-symmetry points within the Brillouin zone, we perform a group-theoretical analysis to derive second-order Raman selection rules. We perform a combined study of second-order selection rules, the calculated phonon dispersion curves, and the phonon density of states (PDOS). This comparison enables us to identify the origins (points within the Brillouin zone from where scattered phonons originate) and nature of second-order events, i.e., whether the observed modes are combinations of single phonons from different dispersion branches or overtones (two phonons from the same branch). Our detailed second-order Raman analysis provides a simultaneous experimental investigation of the

IR- and Raman-active phonons from across the Brillouin zone.

II. MATERIALS AND METHODS

Ga_2O_3 crystal samples with a size of $5 \times 5 \times 0.5 \text{ mm}^3$ used in the present study were prepared from an undoped, two-inch-diameter single crystal grown by the Czochralski method utilizing an Ir crucible and oxidizing growth atmosphere, as described in detail elsewhere [34,35]. The investigated (010)- and $(\bar{2}01)$ -oriented $\beta\text{-Ga}_2\text{O}_3$ crystals received a chemical-mechanical polishing (CMP). The samples are semiconducting with a free-electron concentration and electron mobility of $3.4 \times 10^{17} \text{ cm}^{-3}$ and $118 \text{ cm}^2 \text{ V}^{-1} \text{ s}^{-1}$ according to Hall effect measurements [36]. The investigated Czochralski-grown bulk single crystals exhibit high structural quality, with no twins, low-angle grain boundaries, or nanopipes, while the dislocation density did not exceed values of about $\sim 10^3 \text{ cm}^{-3}$ [37].

Raman scattering at room temperature (293 K) was induced by a 532.16 nm frequency-stabilized single longitudinal mode diode-pumped solid-state (DPSS) laser (Laser Quantum Torus 532) on a LabRAM HR 800 spectrometer (Horiba Jobin-Yvon). The laser beam was focused onto the sample using a $50\times$ Olympus objective with a numerical aperture (NA) of 0.75, with the scattered light being collected in backscattering geometry. Backreflected and elastically scattered light (Rayleigh component) was filtered using an ultralow-frequency filter (ULF) unit and then spectrally dispersed by a monochromator with a grating of 1800 lines/mm (first-order Raman spectroscopy measurements) or 600 lines/mm (second-order Raman spectroscopy measurements). The light was detected by a charge-coupled device (CCD). The spectral dispersion of the setup is $0.35 \text{ cm}^{-1}/\text{pixel}$. Using the 1800 lines/mm grating, the spectral resolution at 550 nm (610 cm^{-1}) is about 0.7 cm^{-1} . The precision in the determination of peak positions in comparison to neighboring Raman modes after line-shape fitting for nonoverlapping modes is better than 0.1 cm^{-1} . The sample was placed beneath the objective with a respective surface's normal parallel to the direction of light propagation. A $\lambda/2$ wave plate in the excitation was set at 0° or 45° to polarize the incident light parallel or crossed with respect to the scattered light, which was selected using a fixed polarizer in the detection. Prior to each measurement, the Raman spectrometer was calibrated using the spectral lines of a neon spectral lamp.

The theoretical results were computed using density functional perturbation theory (DFPT) as implemented into the QUANTUM ESPRESSO suite [38]. The local-density approximation (LDA) to the exchange-correlation interaction has been shown [6,11] to yield a good description of the vibrational spectra of Ga_2O_3 and was thus used for all computations. We also did calculations using the popular PBEsol functions, which yielded a convincing qualitative agreement with the LDA results, albeit with an underestimation of the computed phonon frequencies. We fully optimized the atomic positions and cell parameters until the residual forces between atoms and the cell stress were smaller than $0.001 \text{ eV}/\text{\AA}$ and 0.01 GPa , respectively. The threshold for the total energy was set to 10^{-15} Ry , which ensured tightly converged

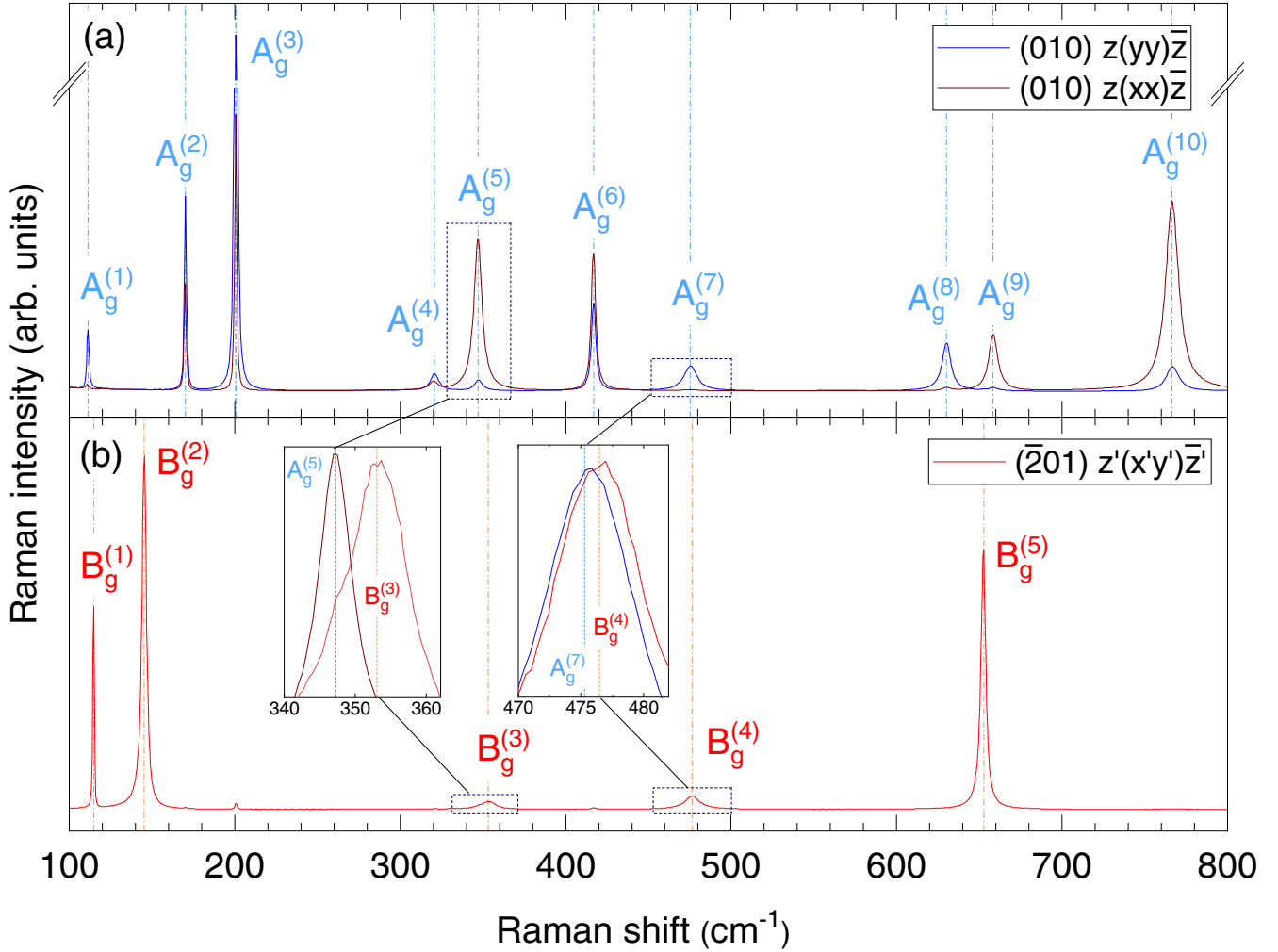


FIG. 1. Raman spectra of the investigated β -Ga₂O₃ single crystal. A_g -modes are obtained by irradiating the (010) plane in parallel polarization, with Cartesian coordinates x , y , and z chosen such that the z -axis aligns with the [010] direction, while $y \parallel [100]$. B_g -modes are acquired by excitation of the $(\bar{2}01)$ plane in crossed polarization. Here, z' points in the direction of the surface normal, with $x' \parallel [010]$ and $y' \parallel [102]$. The insets resolve the closely matching $A_g^{(5)}/B_g^{(3)}$ or $A_g^{(7)}/B_g^{(4)}$ modes with magnified scaling.

interatomic forces and electronic density distributions. The Ga($3d, 4s, 4p$) and O($2s, 2p$) states were treated as valence electrons using multiprojector norm-conserving pseudopotentials from the PseudoDojo library [39] with a cutoff of 180 Ry. All reciprocal space integrations of the electronic structure were performed on a Γ -centered Monkhorst-Pack grid of $8 \times 8 \times 8$ k -points in the Brillouin zone. We then computed the phonon modes and dynamical matrices for phonon momenta on a regular grid of $4 \times 4 \times 4$ q -points. Based on these results, the phonon band structure and corresponding phonon density-of-states (PDOS) were obtained through Fourier interpolation along a chosen path between high-symmetry points and onto a denser grid of $50 \times 50 \times 50$ q -points, respectively.

III. RESULTS AND DISCUSSION

A. First-order Raman scattering

The first-order Raman-active phonon modes of β -Ga₂O₃ are acquired in polarized micro-Raman measurements, the results of which are depicted in Fig. 1.

The monoclinic unit cell (space group: $C_{2h}^3; C2/m$) [10,40–43] is composed of ten atoms: four Ga-atoms (two each in tetrahedral and octahedral coordination) and six O-atoms in between [40]. This implies a total of 30 phonons within the first Brillouin zone, whose irreducible representation at the Γ -point is given by [2,4,5]

$$\Gamma = 10 A_g + 5 B_g + 5 A_u + 10 B_u = \Gamma_{\text{aco}} + \Gamma_{\text{opt}}, \quad (1)$$

where $\Gamma_{\text{aco}} = A_u + 2 B_u$ or $\Gamma_{\text{opt}} = 10 A_g + 5 B_g + 4 A_u + 8 B_u$ refer to the acoustic or optical phonons, respectively. Among the optical phonons, modes with even parity (index g) are Raman-active and can be probed in first-order Raman measurements, whereas modes of odd parity (index u) are IR-active and hence not detectable using first-order Raman spectroscopy. The Raman-active first-order phonon modes of different vibrational symmetries are separated by application of specific polarization geometries as predicted by first-order Raman selection rules (summarized in Table I).

Using the Porto notation, the scattering geometries applied on the (010) plane in parallel polarization [Fig. 1(a)] can be

TABLE I. First-order Raman selection rules for monoclinic crystals in typical backscattering geometries. Polarization configurations are described using the Porto notation. Coordinates x , y , and z are chosen such that y and z align with the $[100]$ or $[010]$ directions, while the x -axis is tilted an angle of 13.8° against the $[001]$ direction. The z' direction points in the direction of the $(\bar{2}01)$ plane's surface normal, with $x' \parallel [010]$ and $y' \parallel [102]$.

Plane	Polarization $\vec{k}_i(\vec{e}_i\vec{e}_s)\vec{k}_s$	Allowed Raman modes
$b/(010)$	$z(yy)\bar{z}, z(xx)\bar{z}$	A_g
$(\bar{2}01)$	$z'(x'x')\bar{z}', z'(y'y')\bar{z}'$	A_g
$(\bar{2}01)$	$z'(x'y')\bar{z}'$	B_g

written as (i) $z(yy)\bar{z}$ (blue) or (ii) $z(xx)\bar{z}$ (brown), where y and z correspond to the $[100]$ or $[010]$ directions, while the x -axis is tilted an angle of 13.8° against the $[001]$ direction (cf. Fig. 1 in Ref. [6]). Selection rules predict the presence of A_g and the absence of B_g modes in these configurations. Conversely, solely B_g modes are available when exciting the $(\bar{2}01)$ plane and selecting a crossed polarization configuration $z'(x'y')\bar{z}'$ [Fig. 1(b)], with $x' \parallel [010]$ and $y' \parallel [102]$. With regard to the measurements on the (010) plane, our data reveal that the (i) $A_g^1, A_g^2, A_g^3, A_g^4, A_g^7,$ and A_g^8 or (ii) $A_g^5, A_g^6, A_g^9,$ and A_g^{10} modes have maximum intensity in the respective geometries, indicating a 90° phase shift between the two races of modes previously observed in angular-resolved Raman scans [1].

The spectral positions of the Raman modes in Fig. 1 are determined by fitting Lorentzian line-shape functions, with the peak positions listed in Table II. Our results show good agreement with previous experimental and theoretical data.

TABLE II. Spectral positions of the monocrystalline β -Ga₂O₃ first-order Raman peaks in Fig. 1, given in cm^{-1} . Peak positions were determined by fitting Lorentzian line-shape functions. The data are compared with the results of DFPT-LDA calculations and previous experimental as well as theoretical results. The results obtained in this work are denoted by †. Where available, the applied exchange correlation functional is specified. A more likely assignment for two peaks from [3] suggested by [1] is indicated by *. - denotes modes that were not observed.

Phonon mode	Experiment						Theory					
	†	[6]	[1]	[2]	[3]	[5]	LDA †	LDA [6]	B3LYP [1]	[2]	LDA [3]	Perdew-Burke-Ernzerhof [4]
A_g^1	111.4	110.7	111.0	111	110.2	112	106.0	106.4	113.5	113	104	104.7
B_g^1	114.8	114.3	114.8	114	113.6	115	107.1	107.7	118.6	114	113	112.1
B_g^2	145.5	144.9	144.8	147	144.7	149	146.6	145.0	145.6	152	149	141.3
A_g^2	170.4	169.8	169.9	169	169.2	173	163.4	163.1	176.4	166	165	163.5
A_g^3	200.9	200.3	200.2	199	200.4	205	191.6	190.5	199.1	195	205	202.3
A_g^4	320.9	320.3	320.0	318	318.6	322	314.9	314.0	318.5	308	317	315.8
A_g^5	347.2	347.0	346.6	346	364.4	350	348.5	345.0	342.5	353	346	339.7
B_g^3	353.5	353.4	353.2	353	-	355	355.2	351.4	359.2	360	356	348.3
A_g^6	417.0	416.7	416.2	415	415.7	421	382.6	384.2	432.0	406	418	420.2
A_g^7	475.6	475.3	474.9	475	-	479	461.7	458.9	472.8	468	467	459.4
B_g^4	476.6	475.9	474.9	475	473.5	480	477.6	473.3	486.1	474	474	472.8
A_g^8	630.4	630.4	630.0	628	628.7*	635	626.0	620.3	624.4	628	600	607.1
B_g^5	652.6	652.4	652.3	651	652.5*	659	647.3	644.4	653.9	644	626	627.1
A_g^9	658.5	659.0	658.3	657	-*	663	652.4	648.5	655.8	654	637	656.1
A_g^{10}	766.9	767.3	766.7	763	763.9	772	754.4	751.5	767.0	760	732	757.7

The vast majority of experimental works do not distinguish between the A_g^7 and B_g^4 modes due to the spectral proximity of these two modes. In fact, only two previous studies [5,6] have reported their individual frequencies. A reliable differentiation between these modes requires sufficiently strong suppression of either A_g or B_g modes by choice of scattering geometry and polarization. In the present study, this can easily be demonstrated by the intensity of the commonly most intense A_g^3 mode in the parallel-polarized scattering geometries on the (010) plane in Fig. 1(a), which is barely visible in the crossed polarized spectra of the $(\bar{2}01)$ plane in Fig. 1(b). Conversely, the most intense B_g^2 mode in Fig. 1(b) is completely absent in Fig. 1(a). Consequently, the positions of closely neighboring modes of different symmetries (A_g^7 and B_g^4 or A_g^5 and B_g^3) can be determined with high confidence without interference of the respective others. In detail, we obtained a frequency difference of 1.0 cm^{-1} between the A_g^7 and B_g^4 modes, which is in line with the previously reported values [5,6] ranging between 0.6 and 1.0 cm^{-1} .

B. Second-order Raman scattering

While momentum and energy conservation restrict first-order Raman scattering to the Γ -point and provide access only to the Raman-active phonon modes, both Raman- and IR-active phonons from across the first Brillouin zone (i.e., with arbitrary wave vectors) participate in two-phonon scattering events. The second-order Raman cross-section and hence the second-order intensity is proportional to the single-phonon density of states, which in turn depends on the phonon dispersion [26,27,30]. A high phonon density of states corresponds to dispersion bands running flat at certain phonon wave vectors \mathbf{q} . Thus, high phonon densities of states within the first

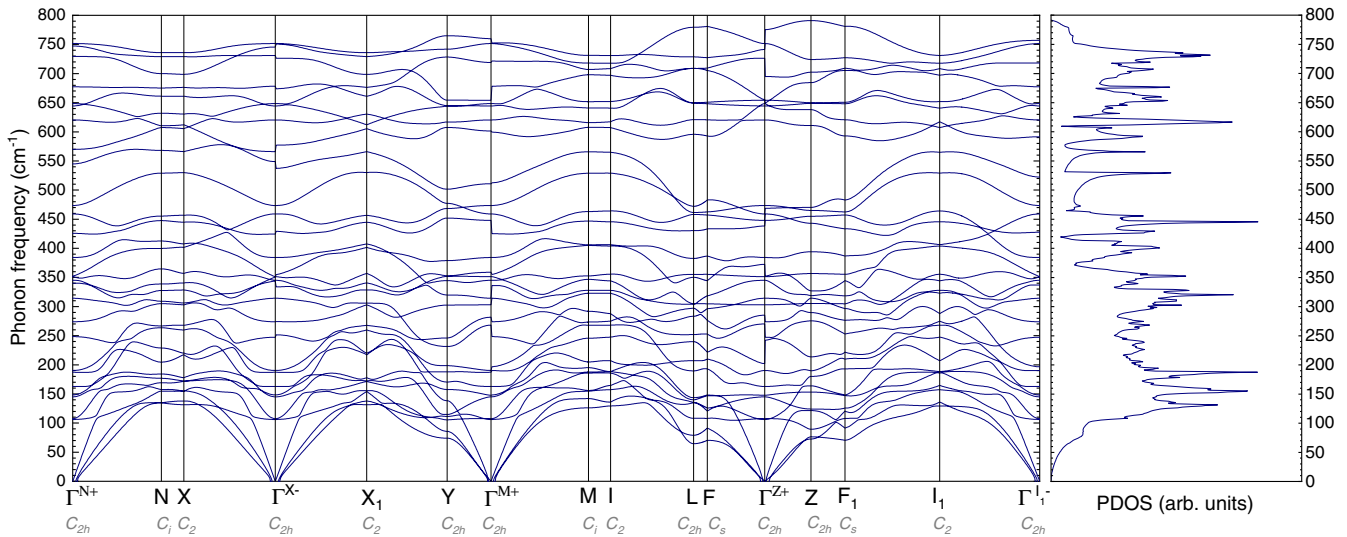


FIG. 2. Calculated phonon dispersion (left) and phonon density of states (right) of monoclinic β -Ga₂O₃. The critical points in the monoclinic unit cell along with the corresponding point group symmetries are illustrated at the bottom of the graph. Individual Γ -points are distinguished by introducing superscripts to label each Γ -point by the inbound (−) or outbound (+) phonon branch direction, e.g., Γ^{X-} or Γ^{X1+} as equivalent labels for the Γ -point between the X and X_1 points. PDOS denotes phonon density of states.

Brillouin zone may be observed at critical points, i.e., high-symmetry points where the phonon dispersion becomes flat. The origins of second-order Raman peaks may be discussed based on the phonon dispersion curves and corresponding single-phonon density of states (PDOS) in combination with second-order Raman selection rules. The dispersion curves and PDOS are illustrated in Fig. 2. For reasons of clarity and simplicity, the symmetries of the individual phonon branches are not indicated, but they are available in Fig. S1 of the Supplemental Material [44]. Polar phonons induce an oscillating macroscopic electric field in the direction of atomic displacements, leading to a splitting of the IR-active A_u and B_u modes into transverse-optical (TO) and longitudinal-optical (LO) phonons [4,16,17]. The nonpolar A_g and B_g modes, in turn, exhibit no LO-TO splitting. The inclusion of the LO-TO splitting into our calculations leads to a steplike behavior in the phonon dispersion for a number of branches at the Γ -point, which is fully consistent with previous theoretical studies [4,45,46].

Since second-order Raman selection rules for monoclinic crystals are presently unavailable, we performed a group-theoretical analysis, the results of which are summarized in Table III. The first column lists the critical points, along with the respective reciprocal space coordinates as determined by a previous work [47], with the second column providing the corresponding point group symmetries.

Due to momentum conservation, each second-order mode originates from a pair of single-phonon modes located at phonon wave vectors of the same absolute value, yet opposing algebraic signs within the Brillouin zone. With regard to the superposition of single-phonon modes, we discriminate (i) overtones and (ii) combinations, in which two phonons from the (i) same or (ii) different phonon branches at the same critical point combine to produce a two-phonon mode at the two phonons' sum or difference frequency. Combinations or overtones are Raman-active (and thus detectable in second-

order Raman measurements) if their reduction to the Γ point contains a Raman-active phonon mode. The Raman-active phonons in the monoclinic crystal structure possess A_g or B_g symmetry, which are detectable using the scattering geometries outlined in Table I. A_g symmetry modes are, for instance, present when irradiating the (010) plane. As a consequence, only those two-phonon modes whose reduction to the Γ -point contains an A_g representation may occur. Four important conclusions can be drawn from Table III.

(i) Two-phonon modes corresponding to an A_g vibrational mode symmetry may originate from all critical points within the Brillouin zone, whereas B_g modes are allowed only for critical points exhibiting a C_2 (I , I_1 , X , and X_1) or C_s (F , F_1) symmetry.

(ii) Overtones always contain the representation A_g .

(iii) Combinations have A_g symmetry if phonons originate from dispersion branches of equal irreducible representation.

(iv) Combinations of phonons from branches corresponding to different irreducible representations occur only in B_g symmetry.

The second-order Raman modes (illustrated in Fig. 3) of β -Ga₂O₃ are obtained in polarized Raman spectroscopy measurements by employing the measurement geometries summarized in Table I, albeit at longer detection times compared to first-order measurements to resolve modes of low intensities. Peak positions of the two-phonon modes in Fig. 3 are likewise obtained by fitting Lorentzian line-shape functions, with the peak positions indicated by dashed vertical lines.

An overview of the recorded second-order Raman frequencies in Fig. 3 and their vibrational symmetries is provided in Table IV. Vibrational symmetries are deduced from the Raman selection rules summarized in Table I, which suggest an A_g or B_g mode symmetry in parallel polarization or crossed polarization. As pointed out earlier, we discriminate overtones and combinations, to which the recorded second-order

TABLE III. Group-theoretical selection rules for two-phonon Raman scattering in monoclinic crystals. BZ or rsc denote “Brillouin zone” or “reciprocal space coordinates.” RSC are chosen based on the primitive monoclinic unit cell suggested in Ref. [47]. The reciprocal space coordinates used here have the following meaning: $\Psi = \frac{3}{4} - b^2/(4a^2\sin^2\beta)$, $\Phi = \Psi - (\frac{3}{4} - \Psi)_c^a \cos\beta$, $\zeta = (2 + \frac{a}{c}\cos\beta)/4 \sin^2\beta$, and $\eta = \frac{1}{2} - 2\zeta \frac{c}{a}\cos\beta$, with $\beta = 103.77^\circ$ denoting the monoclinic angle [40].

Point in the BZ with rsc	Point group symmetry	Irreducible representations for points in the BZ and their correlations	Overtones	Combinations
$\Gamma (0,0,0)$	C_{2h}	$A_g = \Gamma_1$ $B_g = \Gamma_2$ $A_u = \Gamma_3$ $B_u = \Gamma_4$	$[\Gamma_1]^2, [\Gamma_2]^2,$ $[\Gamma_3]^2, [\Gamma_4]^2 \supset A_g$	$\Gamma_1 \times \Gamma_1, \Gamma_2 \times \Gamma_2,$ $\Gamma_3 \times \Gamma_3, \Gamma_4 \times \Gamma_4 \supset A_g$
$Y (-\frac{1}{2}, \frac{1}{2}, 0)$	C_{2h}	$A_g = Y_1$ $B_g = Y_2$ $A_u = Y_3$ $B_u = Y_4$	$[Y_1]^2, [Y_2]^2,$ $[Y_3]^2, [Y_4]^2 \supset A_g$	$Y_1 \times Y_1, Y_2 \times Y_2,$ $Y_3 \times Y_3, Y_4 \times Y_4 \supset A_g$
$L (-\frac{1}{2}, \frac{1}{2}, \frac{1}{2})$	C_{2h}	$A_g = L_1$ $B_g = L_2$ $A_u = L_3$ $B_u = L_4$	$[L_1]^2, [L_2]^2,$ $[L_3]^2, [L_4]^2 \supset A_g$	$L_1 \times L_1, L_2 \times L_2,$ $L_3 \times L_3, L_4 \times L_4 \supset A_g$
$Z (0, 0, \frac{1}{2})$	C_{2h}	$A_g = Z_1$ $B_g = Z_2$ $A_u = Z_3$ $B_u = Z_4$	$[Z_1]^2, [Z_2]^2,$ $[Z_3]^2, [Z_4]^2 \supset A_g$	$Z_1 \times Z_1, Z_2 \times Z_2,$ $Z_3 \times Z_3, Z_4 \times Z_4 \supset A_g$
$M (0, \frac{1}{2}, \frac{1}{2})$	C_i	$\Gamma_{1,2} \rightarrow M_1$ $\Gamma_{3,4} \rightarrow M_2$	$[M_1]^2, [M_2]^2 \supset A_g$	$M_1 \times M_1, M_2 \times M_2 \supset A_g$
$N (0, \frac{1}{2}, 0)$	C_i	$\Gamma_{1,2} \rightarrow N_1$ $\Gamma_{3,4} \rightarrow N_2$	$[N_1]^2, [N_2]^2 \supset A_g$	$N_1 \times N_1, N_2 \times N_2 \supset A_g$
$I (\Phi - 1, \Phi, \frac{1}{2})$	C_2	$\Gamma_{1,3} \rightarrow I_1$ $\Gamma_{2,4} \rightarrow I_2$	$[I_1]^2, [I_2]^2 \supset A_g$	$I_1 \times I_1, I_2 \times I_2 \supset A_g$ $I_1 \times I_2 \supset B_g$
$I_1 (1 - \Phi, 1 - \Phi, \frac{1}{2})$	C_2	$\Gamma_{1,3} \rightarrow I_{11}$ $\Gamma_{2,4} \rightarrow I_{12}$	$[I_{11}]^2, [I_{12}]^2 \supset A_g$	$I_{11} \times I_{11}, I_{12} \times I_{12} \supset A_g$ $I_{11} \times I_{12} \supset B_g$
$X (1 - \Psi, 1 - \Psi, 0)$	C_2	$\Gamma_{1,3} \rightarrow X_1$ $\Gamma_{2,4} \rightarrow X_2$	$[X_1]^2, [X_2]^2 \supset A_g$	$X_1 \times X_1, X_2 \times X_2 \supset A_g$ $X_1 \times X_2 \supset B_g$
$X_1 (\Psi - 1, \Psi, 0)$	C_2	$\Gamma_{1,3} \rightarrow X_{11}$ $\Gamma_{2,4} \rightarrow X_{12}$	$[X_{11}]^2, [X_{12}]^2 \supset A_g$	$X_{11} \times X_{11}, X_{12} \times X_{12} \supset A_g$ $X_{11} \times X_{12} \supset B_g$
$F (\zeta - 1, 1 - \zeta, 1 - \eta)$	C_s	$\Gamma_{1,4} \rightarrow F_1$ $\Gamma_{2,3} \rightarrow F_2$	$[F_1]^2, [F_2]^2 \supset A_g$	$F_1 \times F_1, F_2 \times F_2 \supset A_g$ $F_1 \times F_2 \supset B_g$
$F_1 (-\zeta, \zeta, \eta)$	C_s	$\Gamma_{1,4} \rightarrow F_{11}$ $\Gamma_{2,3} \rightarrow F_{12}$	$[F_{11}]^2, [F_{12}]^2 \supset A_g$	$F_{11} \times F_{11}, F_{12} \times F_{12} \supset A_g$ $F_{11} \times F_{12} \supset B_g$

Raman peaks are allocated (Table IV) using the following algorithm:

(1) If a mode occurs in B_g symmetry, second-order selection rules (Table III) imply that the mode must result from a combinational process occurring at the I , I_1 , X , X_1 , F , or F_1 point.

(2) A_g symmetry modes may originate from either combination or overtone processes at any critical point within the Brillouin zone.

(3) Second-order events are preferably produced by the combination of phonon branches running flat at the critical points within the Brillouin zone, i.e., frequencies characterized by peaks in the PDOS. Thus, if a phonon branch at half the recorded second-order Raman frequency has negligible slope or analogously the PDOS exhibits a peak, the two-phonon mode is likely an overtone. Similarly, two distinctive phonons combine if the sum or difference of their frequencies matches a second-order frequency and the respective phonon

branches run flat or the PDOS exhibits a peak at either of the two frequencies in question.

(4) The second-order selection rules summarized in Table III must be fulfilled for all considered phonon branch combinations and overtones.

In the following, the correlation of a respective second-order mode to its process of creation is illustrated exemplarily for a selection of modes. As a first example, we consider the experimental mode recorded at 1074.3 cm^{-1} . This mode is visible for parallel polarization on the $(\bar{2}01)$ and (010) planes, but forbidden for crossed polarization. Thus, first-order Raman selection rules (Table I) predict that this mode possesses an A_g symmetry. The (2) second-order selection rules (Table III), in turn, provide possible critical points from which single phonons may originate to produce second-order events. When exhibiting an A_g symmetry, a second-order mode may originate from any critical point and be produced by either an overtone or combinational process on the condition that

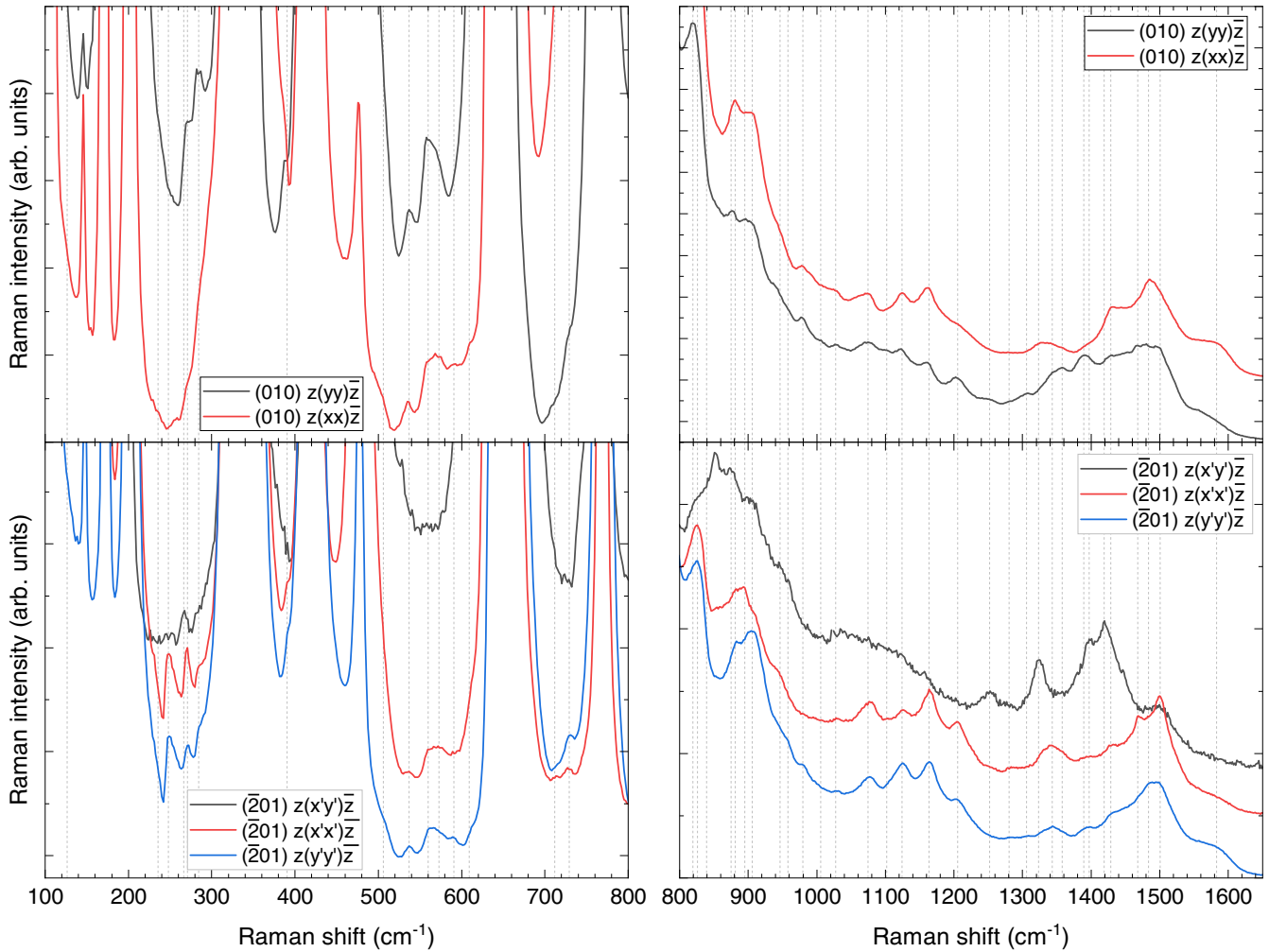


FIG. 3. Second-order Raman spectra of monoclinic β -Ga₂O₃. A_g -modes are obtained by irradiating the (010) and $(\bar{2}01)$ planes in parallel polarization. B_g -modes are acquired by excitation of the $(\bar{2}01)$ plane in crossed polarization. Spectra are vertically offset and scaled to magnify low-intensity modes and allow for a better comparison between individual spectra. The peak positions of second-order modes are determined by fitting Lorentzian line-shape functions, with the peak positions illustrated by vertical dashed lines.

phonon branches exist at the corresponding single-phonon frequencies and these dispersion bands are flat. To investigate whether the observed second-order mode is an overtone or combination of phonons, we consider the (3) PDOS (Fig. 2), which shows an intense peak at about half the recorded second-order frequency. The phonon dispersion branches at the half-frequency exist and run flat at the N , X , X_1 , M , I , and I_1 points (cf. the last column in Table IV). Consequently, the observed two-phonon mode likely stems from an optical overtone process, although, due to the rich panoply of phonon branches, combinational modes may still be superimposed. Similar to the first example, the two-phonon mode recorded at 572 cm^{-1} (Fig. 3) occurs in parallel polarization, thus in A_g symmetry. In contrast to the first example, however, this mode's PDOS exhibits no intense peak at half the recorded frequency, ruling out an optical overtone process. Possible combinations require (3) a pair of phonon branches becoming flat at any of the critical points and the sum (or difference) of their frequencies being equal to the observed two-phonon Raman frequency. In combination with (4) the two-phonon

Raman selection rules (Table III), possible phonon combinations with phonon dispersion branches running flat are evident at the N , M , X , X_1 , I , and I_1 points. A possible combination characterized by dispersion bands running flat paired with a high PDOS (Fig. 2) for the two phonons involved in a sum frequency process is the combination of the lowest-energy acoustic phonon of N_1 symmetry at $\sim 130\text{ cm}^{-1}$ and the IR-active phonon of the same symmetry predicted at $\sim 448\text{ cm}^{-1}$. Due to the high number of phonon branches, we do not explicitly list all possible origins of combinations in Table IV, but we limit ourselves to the origins of overtone processes in the following.

The second-order modes in the two previous examples occurred in parallel polarization and hence possess an A_g symmetry. Conversely, modes observed in crossed polarization on the $(\bar{2}01)$ plane have B_g symmetry. An intense B_g symmetry second-order mode is located at $\sim 851.9\text{ cm}^{-1}$ (cf. Fig. 3 and Table IV). For B_g symmetry, (1) second-order selection rules (Table III) predict that the second-order mode must stem from a combinational process occurring at the I , I_1 , X , X_1 , F , or F_1

TABLE IV. Raman frequencies, vibrational symmetries, processes leading to two-phonon events, and origins within the Brillouin zone of β -Ga₂O₃ second-order Raman modes observed in Fig. 3. The observed peaks are allocated to the two-phonon process and the origin of scattering event in the Brillouin zone. Possible origins of overtone processes are listed. Γ -point overtones are labeled by accounting for the inbound or outbound phonon dispersion branch directions as explained in Fig. 2. As an example, a phonon branch possessing a Γ_1 symmetry at the Γ^{Z+} point is referred to as Γ_1^{Z+} .

Raman shift (cm ⁻¹)	Vibrational symmetry	Process	Origin in the Brillouin zone
126.3	A_g	combination	
235.4	A_g	optical/acoustic overtone or combination	$[Y_4]^2$ (optical), $[Z_4]^2$ (acoustic)
248.0	A_g	combination	
266.4	B_g	combination	
271.0	A_g	acoustic overtone or combination	$[N_2]^2, [X_2]^2, [X_{11}]^2$
284.2	A_g	optical overtone or combination	$[M_2]^2$
390.6	A_g	optical overtone or combination	$[Y_1]^2, [M_1]^2, [L_1]^2, [F_1]^2, [Z_4]^2, [F_{11}]^2, [I_{11}]^2$
506.4	A_g	optical overtone or combination	$[L_4]^2$
536.7	A_g	optical overtone or combination	$[N_2]^2, [X_2]^2, [M_1]^2, [L_2]^2, [I_{12}]^2$
560.0	A_g	combination	
572.7	A_g	combination	
590.5	A_g	combination	
609.3	A_g	optical overtone or combination	$[N_1]^2, [X_1]^2, [X_2]^2, [X_{11}]^2, [Y_2]^2, [L_4]^2, [F_2]^2, [\Gamma_3^{Z+}]^2, [Z_2]^2, [F_{12}]^2$
711.8	A_g	optical overtone or combination	$[\Gamma_1^{Z+}]^2, [Y_3]^2, [M_1]^2, [L_2]^2, [L_2]^2, [F_2]^2, [Z_2]^2, [F_{12}]^2, [I_{12}]^2$
728.1	A_g	combination	
819.2	A_g or B_g	optical overtone or combination	$[N_2]^2, [M_1]^2, [M_2]^2, [I_1]^2, [L_2]^2, [I_{12}]^2$
826.2	A_g	optical overtone or combination	$[N_2]^2, [M_1]^2, [M_2]^2, [I_1]^2, [L_2]^2, [I_{12}]^2$
851.9	B_g	combination	
874.9	B_g	combination	
881.0	A_g	optical overtone	$[N_1]^2, [X_1]^2, [X_2]^2, [M_2]^2, [I_1]^2, [I_{11}]^2$
895.8	A_g	optical overtone	$[N_1]^2, [X_2]^2, [Y_2]^2, [M_2]^2, [I_1]^2, [I_{11}]^2$
907.9	A_g	optical overtone or combination	$[N_2]^2, [X_1]^2, [X_{11}]^2, [\Gamma_3^{X-}]^2, [Y_2]^2, [M_2]^2, [I_1]^2, [L_2]^2, [F_2]^2, [Z_3]^2, [F_{12}]^2$
946.2	A_g or B_g	optical overtone or combination	$[\Gamma_2^{Z+}]^2, [Z_1]^2$
957.5	A_g	optical overtone or combination	$[\Gamma_1^{M+}]^2, [\Gamma_2^{Z+}]^2, [F_{11}]^2$
979.5	A_g	combination	
1005.8	A_g	combination	
1027.6	A_g	combination	
1074.3	A_g	optical overtone or combination	$[N_1]^2, [X_2]^2, [X_{12}]^2, [M_1]^2, [L_2]^2, [I_{12}]^2$
1102.0	A_g	combination	
1124.3	A_g	optical overtone	$[N_2]^2, [X_1]^2, [M_2]^2, [I_1]^2, [I_{11}]^2$
1163.4	A_g	combination	
1205.0	A_g	optical overtone or combination	$[N_1]^2, [M_2]^2, [L_2]^2$
1251.8	B_g	combination	
1280.3	A_g	overtone or combination	$[X_1]^2, [M_2]^2, [I_1]^2, [Z_4]^2, [I_{11}]^2$
1305.4	A_g	optical overtone	$[\Gamma_1^{Z+}]^2, [M_1]^2, [L_2]^2, [F_2]^2, [F_{12}]^2, [I_{12}]^2, [Z_3]^2, [Z_4]^2$
1323.6	B_g	combination	
1343.5	A_g	optical overtone or combination	$[N_2]^2, [X_2]^2, [X_{12}]^2$
1357.7	A_g	optical overtone	$[N_2]^2, [X_2]^2, [X_{12}]^2$
1389.0	A_g	optical overtone or combination	$[N_1]^2, [X_1]^2, [I_1]^2, [M_2]^2, [L_2]^2$
1397.0	B_g	combination	
1418.8	B_g	combination	
1428.2	A_g	optical overtone or combination	$[M_1]^2, [I_1]^2, [I_{11}]^2$
1468.0	A_g	optical overtone	$[N_1]^2, [N_2]^2, [X_1]^2, [X_2]^2, [X_{11}]^2, [X_{12}]^2, [Y_1]^2, [Y_4]^2, [I_{12}]^2$
1483.9	A_g	optical overtone	$[N_1]^2, [X_1]^2, [X_{11}]^2, [Y_1]^2$
1500.5	A_g	optical overtone	$[\Gamma_1^{X-}]^2, [\Gamma_4^{M+}]^2$
1582.8	A_g	optical overtone	$[L_1]^2, [Z_4]^2$

point. A possible sum frequency combination characterized by a high (3) PDOS of the individual single phonons involves the calculated modes at ~ 154 and ~ 676 cm^{-1} . A possible combination allowed by (4) second-order selection rules (Table III) is $X_1 \times X_2$ at the X point.

By applying the algorithm explained above, we investigate the processes leading to the more than 40 observed second-order Raman peaks (Fig. 3), and we list our findings in Table IV. We note that the comparison of the Raman spectra obtained for the Czochralski-grown single crystals with various homoepitaxially grown MBE- and MOCVD-grown films as well as EFG-grown bulk single crystals (Novel Crystal Technology, Inc.) yielded reproducible spectra without indications of defect-related Raman peaks in the spectral range up to 800 cm^{-1} .

While determining the vibrational symmetries is feasible for the vast majority of two-phonon modes, the two peaks observed at 819.2 and 946.2 cm^{-1} occurred in both A_g and B_g measurement configurations. We hence list both vibrational symmetries for these two modes in Table IV. In the case of B_g symmetry, the creation process is strictly combinational, whereas in A_g symmetry both combinations and overtones may contribute. Moreover, the high number of phonon branches within the first Brillouin zone makes the allocation of two-phonon modes to each pair of first-order dispersion branches a challenging endeavor. As stated earlier, overtones and combinations may be superimposed provided that the PDOS is intense or the phonon branches run flat at the respective single-phonon frequencies. Nevertheless, the four highest-frequency second-order Raman modes (> 1468 cm^{-1}) can, for lack of single-phonon branches in the frequency region above 730 cm^{-1} , clearly be attributed to optical overtone processes. Similarly, acoustic overtones as well as combinations of optical-optical and optical-acoustic phonons are seen in the second-order modes of lower or medium frequencies, also providing access to IR or acoustic modes.

IV. CONCLUSIONS

We have reported a combined study of polarized micro-Raman spectroscopy and density functional perturbation theory calculations to investigate the first- and second-order Raman spectra of β - Ga_2O_3 . First, the frequencies of all 15 Raman-active first-order phonons were obtained, with the frequency difference between the closely matching A_g^7 and B_g^4 modes being determined to 1.0 cm^{-1} . Second, the recorded second-order Raman spectra were analyzed in conjunction with the calculated phonon dispersion, phonon density of states, and the derived group-theoretical selection rules for two-phonon scattering. In detail, we identified more than 40 second-order modes and attributed their origins to phonon overtone or combination processes. While modes of B_g symmetry always originate from phonon branch combinations, A_g modes may be both overtones and combinations. This work enables the identification of phonon scattering processes in monoclinic β - Ga_2O_3 from the entire Brillouin zone, and it provides access to both IR- and Raman-active phonons via Raman spectroscopy. Furthermore, the work can serve as a template for the investigation of second-order Raman scattering processes in other monoclinic materials.

ACKNOWLEDGMENTS

We acknowledge funding by the Deutsche Forschungsgemeinschaft (DFG, German Research Foundation)—Project No. 446185170. This work was performed in part in the framework of GraFOx, a Leibniz-ScienceCampus partially funded by the Leibniz association. Computational resources used for the calculations were provided by the HPC of the Regional Computer Centre Erlangen (RRZE). Klaus Irmscher (Leibniz-Institut für Kristallzüchtung) is appreciated for a critical reading of the manuscript.

-
- [1] C. Kranert, C. Sturm, R. Schmidt-Grund, and M. Grundmann, Raman tensor elements of β - Ga_2O_3 , *Sci. Rep.* **6**, 35964 (2016).
 - [2] D. Dohy, G. Lucazeau, and A. Revcolevschi, Raman spectra and valence force field of single-crystalline β - Ga_2O_3 , *J. Solid State Chem.* **45**, 180 (1982).
 - [3] D. Machon, P. F. McMillan, B. Xu, and J. Dong, High-pressure study of the β -to- α transition in Ga_2O_3 , *Phys. Rev. B* **73**, 094125 (2006).
 - [4] B. Liu, M. Gu, and X. Liu, Lattice dynamical, dielectric, and thermodynamic properties of β - Ga_2O_3 from first principles, *Appl. Phys. Lett.* **91**, 172102 (2007).
 - [5] T. Onuma, S. Fujioka, T. Yamaguchi, Y. Itoh, M. Higashiwaki, K. Sasaki, T. Masui, and T. Honda, Polarized Raman spectra in β - Ga_2O_3 single crystals, *J. Cryst. Growth* **401**, 330 (2014).
 - [6] B. M. Janzen, P. Mazzolini, R. Gillen, A. Falkenstein, M. Martin, H. Tornatzky, J. Maultzsch, O. Bierwagen, and M. R. Wagner, Isotopic study of Raman active phonon modes in β - Ga_2O_3 , *J. Mater. Chem. C* **9**, 2311 (2021).
 - [7] K. Zhang, Z. Xu, S. Zhang, H. Wang, H. Cheng, J. Hao, J. Wu, and F. Fang, Raman and photoluminescence properties of un-/ion-doped β - Ga_2O_3 single-crystals prepared by edge-defined film-fed growth method, *Physica B* **600**, 412624 (2021).
 - [8] K. Zhang, Z. Xu, J. Zhao, H. Wang, J. Hao, S. Zhang, H. Cheng, and B. Dong, Temperature-dependent Raman and photoluminescence of β - Ga_2O_3 doped with shallow donors and deep acceptors impurities, *J. Alloys Compd.* **881**, 160665 (2021).
 - [9] Y. Yao, Y. Ishikawa, and Y. Sugawara, X-ray diffraction and Raman characterization of β - Ga_2O_3 single crystal grown by edge-defined film-fed growth method, *J. Appl. Phys.* **126**, 205106 (2019).
 - [10] I. Cora, F. Mezzadri, F. Boschi, M. Bosi, M. Čaplovičová, G. Calestani, I. Dódon, B. Pécz, and R. Fornari, The real structure of ϵ - Ga_2O_3 and its relation to the κ -phase, *CrystEngComm* **19**, 1509 (2017).

- [11] B. M. Janzen, P. Mazzolini, R. Gillen, V. F. S. Peltason, L. P. Grote, J. Maultzsch, R. Fornari, O. Bierwagen, and M. R. Wagner, Comprehensive Raman study of orthorhombic κ/ϵ -Ga₂O₃ and the impact of rotational domains, *J. Mater. Chem. C* **9**, 14175 (2021).
- [12] A. Fiedler, M. Ramsteiner, Z. Galazka, and K. Irmscher, Raman scattering in heavily donor doped β -Ga₂O₃, *Appl. Phys. Lett.* **117**, 152107 (2020).
- [13] P. Seyidov, M. Ramsteiner, Z. Galazka, and K. Irmscher, Resonant electronic Raman scattering from Ir⁴⁺ ions in β -Ga₂O₃, *J. Appl. Phys.* **131**, 035707 (2022).
- [14] C. Kranert, C. Sturm, R. Schmidt-Grund, and M. Grundmann, Raman Tensor Formalism for Optically Anisotropic Crystals, *Phys. Rev. Lett.* **116**, 127401 (2016).
- [15] T. Onuma, S. Saito, K. Sasaki, K. Goto, T. Masui, T. Yamaguchi, T. Honda, A. Kuramata, and M. Higashiwaki, Temperature-dependent exciton resonance energies and their correlation with IR-active optical phonon modes in β -Ga₂O₃ single crystals, *Appl. Phys. Lett.* **108**, 101904 (2016).
- [16] M. Schubert, R. Korlacki, S. Knight, T. Hofmann, S. Schöche, V. Darakchieva, E. Janzén, B. Monemar, D. Gogova, Q.-T. Thieu, R. Togashi, H. Murakami, Y. Kumagai, K. Goto, A. Kuramata, S. Yamakoshi, and M. Higashiwaki, Anisotropy, phonon modes, and free charge carrier parameters in monoclinic β -gallium oxide single crystals, *Phys. Rev. B* **93**, 125209 (2016).
- [17] K. A. Mengle and E. Kioupakis, Vibrational and electron-phonon coupling properties of β -Ga₂O₃ from first-principles calculations: Impact on the mobility and breakdown field, *AIP Adv.* **9**, 015313 (2019).
- [18] E. Villora, Y. Morioka, T. Atou, T. Sugawara, M. Kikuchi, and T. Fukuda, Infrared reflectance and electrical conductivity of β -Ga₂O₃, *Phys. Status Solidi A* **193**, 187 (2002).
- [19] J. L. Birman, Space group selection rules: Diamond and zinc blende, *Phys. Rev.* **127**, 1093 (1962).
- [20] L. Kleinman, Polarization effects in two-phonon Raman scattering in cubic crystals, *Solid State Commun.* **3**, 47 (1965).
- [21] J. H. Parker, D. W. Feldman, and M. Ashkin, Raman scattering by silicon and germanium, *Phys. Rev.* **155**, 712 (1967).
- [22] B. A. Weinstein and M. Cardona, Second-order Raman spectrum of germanium, *Phys. Rev. B* **7**, 2545 (1973).
- [23] B. Weinstein, J. Renucci, and M. Cardona, Effect of hydrostatic pressure on the second order Raman spectrum of GaP, *Solid State Commun.* **12**, 473 (1973).
- [24] P. Mishra and K. P. Jain, First- and second-order Raman scattering in nanocrystalline silicon, *Phys. Rev. B* **64**, 073304 (2001).
- [25] J. M. Calleja and M. Cardona, Resonant Raman scattering in ZnO, *Phys. Rev. B* **16**, 3753 (1977).
- [26] S. Murugkar, R. Merlin, A. Botchkarev, A. Salvador, and H. Morkoç, Second order Raman spectroscopy of the wurtzite form of GaN, *J. Appl. Phys.* **77**, 6042 (1995).
- [27] H. Siegle, G. Kaczmarczyk, L. Filippidis, A. P. Litvinchuk, A. Hoffmann, and C. Thomsen, Zone-boundary phonons in hexagonal and cubic GaN, *Phys. Rev. B* **55**, 7000 (1997).
- [28] V. Y. Davydov, Y. E. Kitaev, I. N. Goncharuk, A. N. Smirnov, J. Graul, O. Semchinova, D. Uffmann, M. B. Smirnov, A. P. Mirgorodsky, and R. A. Evarestov, Phonon dispersion and Raman scattering in hexagonal GaN and AlN, *Phys. Rev. B* **58**, 12899 (1998).
- [29] U. Habocek, H. Siegle, A. Hoffmann, and C. Thomsen, Lattice dynamics in GaN and AlN probed with first- and second-order Raman spectroscopy, *Phys. Status Solidi C* **0**, 1710 (2003).
- [30] H. Gao, F. Yan, H. Zhang, J. Li, J. Wang, and J. Yan, First and second order Raman scattering spectroscopy of nonpolar a-plane GaN, *J. Appl. Phys.* **101**, 103533 (2007).
- [31] B. C. Hu, N. Zhou, Q. Y. Zhang, and C. Y. Ma, Multiphonon resonant Raman scattering and the second-order Raman processes in the excitonic luminescence of ZnO, *Appl. Phys. Lett.* **115**, 142103 (2019).
- [32] Z. Galazka, R. Uecker, K. Irmscher, M. Albrecht, D. Klimm, M. Pietsch, M. Brützmam, R. Bertram, S. Ganschow, and R. Fornari, Czochralski growth and characterization of β -Ga₂O₃ single crystals, *Cryst. Res. Technol.* **45**, 1229 (2010).
- [33] Z. Galazka, K. Irmscher, R. Uecker, R. Bertram, M. Pietsch, A. Kwasniewski, M. Naumann, T. Schulz, R. Schewski, D. Klimm, and M. Bickermann, On the bulk β -Ga₂O₃ single crystals grown by the Czochralski method, *J. Cryst. Growth* **404**, 184 (2014).
- [34] Z. Galazka, R. Uecker, D. Klimm, K. Irmscher, M. Naumann, M. Pietsch, A. Kwasniewski, R. Bertram, S. Ganschow, and M. Bickermann, Scaling-Up of Bulk β -Ga₂O₃ Single Crystals by the Czochralski Method, *ECS J. Solid State Sci. Technol.* **6**, Q3007 (2017).
- [35] Z. Galazka, S. Ganschow, K. Irmscher, D. Klimm, M. Albrecht, R. Schewski, M. Pietsch, T. Schulz, A. Dittmar, A. Kwasniewski, R. Grueneberg, S. B. Anooz, A. Popp, U. Juda, I. M. Hanke, T. Schroeder, and M. Bickermann, Bulk single crystals of β -Ga₂O₃ and Ga-based spinels as ultra-wide bandgap transparent semiconducting oxides, *Prog. Cryst. Growth Charact. Mater.* **67**, 100511 (2021).
- [36] K. Irmscher, Z. Galazka, M. Pietsch, R. Uecker, and R. Fornari, Electrical properties of Ga₂O₃ single crystals grown by the Czochralski method, *J. Appl. Phys.* **110**, 063720 (2011).
- [37] Z. Galazka, Growth of bulk β -Ga₂O₃ single crystals by the Czochralski method, *J. Appl. Phys.* **131**, 031103 (2022).
- [38] P. Giannozzi, S. Baroni, N. Bonini, M. Calandra, R. Car, C. Cavazzoni, D. Ceresoli, G. L. Chiarotti, M. Cococcioni, I. Dabo, A. D. Corso, S. de Gironcoli, S. Fabris, G. Fratesi, R. Gebauer, U. Gerstmann, C. Gougoussis, A. Kokalj, M. Lazzeri, L. Martin-Samos *et al.*, Quantum espresso: A modular and open-source software project for quantum simulations of materials, *J. Phys.: Condens. Matter* **21**, 395502 (2009).
- [39] M. J. van Setten, M. Giantomassi, E. Bousquet, M. J. Verstraete, D. R. Hamann, X. Gonze, and G.-M. Rignanese, The PseudoDojo: Training and grading a 85 element optimized norm-conserving pseudopotential table, *Comput. Phys. Commun.* **226**, 39 (2018).
- [40] J. Furthmüller and F. Bechstedt, Quasiparticle bands and spectra of Ga₂O₃ polymorphs, *Phys. Rev. B* **93**, 115204 (2016).
- [41] S. Yoshioka, H. Hayashi, A. Kuwabara, F. Oba, K. Matsunaga, and I. Tanaka, Structures and energetics of Ga₂O₃ polymorphs, *J. Phys.: Condens. Matter* **19**, 346211 (2007).
- [42] K. Yamaguchi, First principles study on electronic structure of β -Ga₂O₃, *Solid State Commun.* **131**, 739 (2004).

- [43] J. Åhman, G. Svensson, and J. Albertsson, A reinvestigation of β -gallium oxide, *Acta Crystallogr. C* **52**, 1336 (1996).
- [44] See Supplemental Material at <http://link.aps.org/supplemental/10.1103/PhysRevMaterials.6.054601> for the calculated phonon dispersion, phonon density of states, and used lattice parameters of monoclinic β -Ga₂O₃.
- [45] M. D. Santia, N. Tandon, and J. D. Albrecht, Lattice thermal conductivity in β -Ga₂O₃ from first principles, *Appl. Phys. Lett.* **107**, 041907 (2015).
- [46] M. Schubert, A. Mock, R. Korlacki, S. Knight, B. Monemar, K. Goto, Y. Kumagai, A. Kuramata, Z. Galazka, G. Wagner, M. J. Tadjer, V. D. Wheeler, M. Higashiwaki, and V. Darakchieva, Phonon Properties, in *Springer Series in Materials Science* (Springer, Cham, 2020), Vol. 293, pp. 501–534.
- [47] H. Peelaers and C. G. Van de Walle, Brillouin zone and band structure of β -Ga₂O₃, *Phys. Status Solidi B* **252**, 828 (2015).